JSR Publications

Available Online

J. Sci. Res. **18** (2), 251-263 (2026)

**JOURNAL OF SCIENTIFIC RESEARCH**

www.banglajol.info/index.php/JSR

# Reactively Evaporated p-type $Pb_{3.58}Sb_{4.42}Se_{10}$ Thin Film: A Candidate for Photovoltaic and Thermoelectric Applications

**A. T. Namitha[1,*] , K. S. Urmila[2], B. Pradeep[3]**

[1]Department of Physics, Sree Narayana College Nattika, University of Calicut, 680566, India

[2]Department of Physics, S N M College Malienkara, Mahathma Gandhi University, 683516, India

[3]Department of Physics, Cochin University of Science and Technology, 682022, India

Received 11 September 2025, accepted in final revised form 22 February 2026

**Abstract**

For the first time it is reported that thin films of $Pb_{3.58}Sb_{4.42}Se_{10}$ are prepared using reactive evaporation technique under optimized deposition conditions. As prepared films are preliminarily characterized using X-ray Diffraction, X-ray photoelectron spectroscopy , Atomic Force Microscopy and Scanning Electron Microscope. The X-ray diffraction analysis give various structural parameters such as particle size, number of crystallites per unit area, lattice strain and dislocation density and are found to be 25 nm, $3.84\times10^{14}$ $m^{-2}$, $2.267\times10^{-3}$ and $1.6\times10^{15}$ lines $m^{-2}$ respectively. The AFM images indicate that the film consists of very close packed grains with grain size varying between 60 nm and 90 nm. On the basis of transmission spectra, the optical band gap is calculated and found to be about 1.31 eV with direct allowed transition. The Urbach energy, related to the width of band tail of localized states at the band edge is determined and is found to be 0.5 eV. The slow non-exponential decay of photoconductivity with time at room temperature are the characteristics of the continuous distribution of localized states in the material. Low temperature thermoelectric power (TEP) measurements indicate the *p*-type conductivity for the film with Seebeck Coefficient of about 1691 $\mu VK^{-1}$ at room temperature.

***Keywords*:** Lead antimony selenide thin films; Reactive evaporation; Thermoelectric studies.


doi: https://dx.doi.org/10.3329/jsr.v18i2.84258 J. Sci. Res. **18** (2), 251-263 (2026)

## 1. Introduction

Since solar energy is readily available and most stable, in contrast to wind, water and pressure, the utilization of full spectrum solar energy, in order to mitigate the global energy crisis, through the optimal hybridization of photovoltaic (PV) and thermoelectric (TE) devices is in demand [1]. Thermoelectric devices are silent, reliable and scalable rather than their efficiency, making them ideal for small, distributed power generation and refrigeration applications. Thermoelectric material efficiency is given by the dimensionless figure of merit $ZT = \frac{S^2\sigma T}{\mathcal{K}}$ or power factor $P = S^2\sigma$ where $S$ is the Seebeck coefficient, $\sigma$ is the

* *Corresponding author*: namithaprijith@gmail.com

electrical conductivity and $\mathcal{K}$ is the thermal conductivity. The figure of merit can be increased by maximizing the power factor through and/or minimizing the thermal conductivity. The power factor maximization can be achieved through the development of newly developed materials, optimization of existing materials by doping, and the exploration of nanoscale materials. The thermal conductivity can be minimized by alloying and/or nanostructuring [2]. Initially the materials used for commercial applications include bulk $Bi_2Te_3$, PbTe, SiGe system [3]. Some of the recently developed materials under investigation include skutterudites [4-6], clathrates [7-10], half-Heusler alloys [11-13], complex chalcogenides [14-17], complex oxide materials [18], thin film superlattice structures [19] and nano structured materials [20-23]. The thin film thermoelectric devices will enhance thermoelectric performance because (i) films have lower thermal conductivity than those of bulk materials due to strong phonons scattering at surfaces and film-surface interface and (ii) density of states near the Fermi energy is enhanced, giving rise to increased Seebeck coefficient [24,25].

The low efficiency and high price of solar cell materials have limited their widespread application. Since most of the chalcogenide compounds are environmentally stable, high melting points and have energy gaps appropriate for photovoltaic applications over a wide range of temperatures, these compounds have had a prominent position in the field of photovoltaic. Polycrystalline thin films of copper indium sulphide ($CuInS_2$), copper gallium sulphide ($CuGaS_2$), copper indium gallium diselenide ($Cu(In,Ga)Se_2$), copper gallium indium sulfide ($CuGaInS_2$), cadmium telluride (CdTe), cadmium sulphide (CdS), indium diselenide ($InSe_2$) and copper indium aluminum diselenide (CIAS) are the chalcogenide materials that have been extensively studied for photovoltaic applications [26]. The key issue of micro-electronic devices is the fabrication of new and novel semiconducting thin films with high opto-electronic and thermoelectric properties for small-scale solar energy conversion applications.

Here nano-structured p-type lead antimony selenide ($Pb_{3.58}Sb_{4.42}Se_{10}$) thin films have been prepared using reactively evaporation technique and their structural, optical, electrical and transient photoconductivity properties are evaluated. Interest in extending the temperature range of operation above that of the commercially used TE materials, the Seebeck coefficient of thin films are studied over 11-300K.

## 2. Experimental Details

Thin films of p-type lead antimony selenide ($Pb_{3.58}Sb_{4.42}Se_{10}$) were prepared by using reactive evaporation technique on to ultrasonically cleaned glass substrates kept at 448±5K. The synthesize of thin film compound from the elements prior to deposition which is a tedious and sometimes expensive metallurgical process which is eliminated in this technique. The compound will be decomposed upon heating in vacuum due to large differences in the vapor pressure of lead, antimony and selenium and consequent lack of stoichiometry in the films are avoided. In this work, antimony (purity 99.999%) and selenium (purity 99.999 %) were evaporated from two separate glass crucibles kept in

molybdenum baskets and lead (purity 99.999 %) from a molybdenum boat. The source materials were heated with current at vacuum ~$10^{-5}$ torr, evaporated and deposited on glass substrates at 448±5K. The optimized parameters used for the preparation of the samples in present wok are given below (Table 1).

Table 1. Deposition parameters.

| | |
|---|---|
| Impingement rate of lead | ≈ $1.13\times10^{15}$ atoms $cm^{-2}$ $s^{-1}$ |
| Impingement rate of antimony | ≈ $2\times10^{15}$ atoms $cm^{-2}$ $s^{-1}$ |
| Impingement rate of selenium | ≈ $6\times10^{14}$ atoms $cm^{-2}$ $s^{-1}$ |
| Substrate temperature | = 448 ± 5 K |

The prepared film is found to be a thickness of about 600 nm. It was measured using stylus profiler (Dektak 6M stylus profiler). The XRD measurements were done using Rigaku D MaxC X-Ray Diffractometer with Cu-Kα radiation. To determine the morphology and microstructure of the film, SEM (JEOL Model JSM-6390 LV) and AFM (AFM nanoscope E, Digital Instruments) were used, XPS - VSW Scientific Instruments - photoelectron spectrometer using monochromatic Al-Kα radiation (1486.6 eV) was used for XPS measurements. JASCO V-570 UV-Vis-NIR spectrophotometer was used for recording the optical transmittance spectra of the films The photo conductivity and dark conductivity of the films was recorded using a Keithley 2611A source meter, a bias voltage of 10 V was applied and current was recorded in the dark for 150 s and under illumination (FSH lamp of 82 V, 300 W) for another 300 s. The thermoelectric properties of the film was measured in the temperature range of 11-300 K. ECOPIA HMS-3000 system is used for Hall measurements.

## 3. Results and Discussion

### 3.1. *Structural analysis*

Fig. 1. shows the XRD pattern of the as prepared film which reveals the polycrystalline nature of $Pb_{3.58}Sb_{4.42}Se_{10}$ thin film. All peaks are indexed as per ICDD file no: 80-0654 (Table 2). The absence of 100 % peak in the prepared film as that of standard pattern may be due to the orientation of the (521) plane perpendicular to the film surface. The XRD peaks shows an orthorhombic structure with lattice parameters a = 24.77Å, b = 20.25Å, c = 4.12Å and molecular weight = 2069.51 which are consistent with the ICDD file no: 80-0654 [27].

Table 2. The observed XRD data along with standard ICDD data.

| Standard pattern (ICDD Card No: 80-0654) | | | As prepared film | |
|---|---|---|---|---|
| (hkl) | d(Å) | $I/I_0$ | d(Å) | $I/I_0$ |
| 230 | 5.8053 | 2 | 5.9272 | 8 |
| 420 | 5.2195 | 1 | 5.2787 | 10 |
| 360 | 3.0555 | 24 | 3.05901 | 100 |
| 521 | 3.0260 | 100 | - | - |
| 920 | 2.6334 | 1 | 2.63357 | 8 |

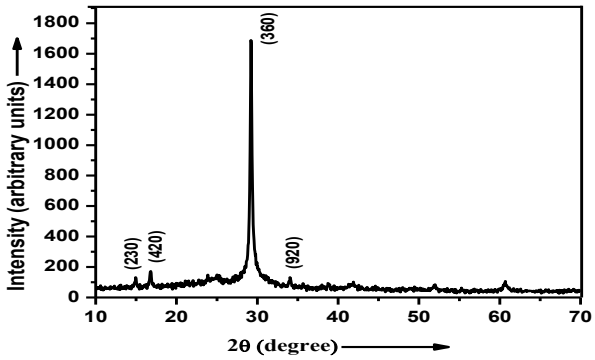


Fig. 1. X-ray diffraction pattern of a typical $Pb_{3.58}Sb_{4.42}Se_{10}$ sample.

The calculated values of particle size, dislocation density, number of crystallites per unit area and strain in the as prepared are shown in Table 3 [28].

Table 3. Microstructural parameters.

| | |
|---|---|
| Average particle size D (nm) | ~25 |
| Dislocation density $\rho$ (lines $m^{-2}$) | ~$1.6\times10^{15}$ |
| Number of crystallite per unit area $N$ ($m^{-2}$) | ~$3.84\times10^{14}$ |
| Strain $T$ | ~$2.267\times10^{-3}$ |

### 3.2. *Morphological and compositional analysis*

The SEM image of a typical $Pb_{3.58}Sb_{4.42}Se_{10}$ thin film with 5,000 magnifications is shown in Fig. 2. Figure shows that the film is composed of minute grains without cracks or pinholes and it well covers the glass substrate. The EDS spectra of the thin films as depicted in Fig. 3 show that the sample consists of lead, antimony and selenium.

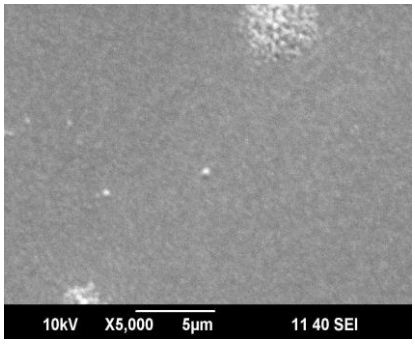


Fig. 2. Surface morphology of lead antimony selenide thin film.

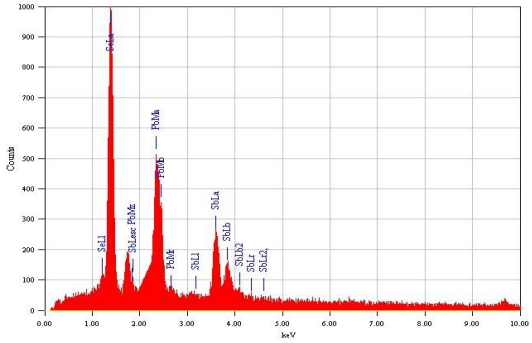


Fig. 3. EDAX spectra of a typical lead antimony selenide thin film.

X-ray photoelectron spectra of Pb 4f, Sb 3d and Se 3d for a typical $Pb_{3.58}Sb_{4.42}Se_{10}$ thin film are shown in Figs. 4(a)-(c). The Pb $4f_{7/2}$ and $4f_{5/2}$ peaks shown in Fig. 4(a) are centered at about 137.03 eV and 142.07 eV. These peaks are attributed to the possible presence of lead in $Pb_{3.58}Sb_{4.42}Se_{10}$ film. The binding energies of Sb $3d_{3/2}$ and Sb $3d_{5/2}$ peaks (Fig. 4(b)) are observed at about 540.1 eV and 530.82 eV respectively. The Se $3d_{5/2}$ peak is shown in Fig. 4(c) with binding energies of about 53.29 eV. Compositional analysis gives result as 20 % of Pb, 35 % of Sb and 45 % of Se which confirms the films are nearly stoichiometric. The above results confirm the formation of $Pb_{3.58}Sb_{4.42}Se_{10}$ film.

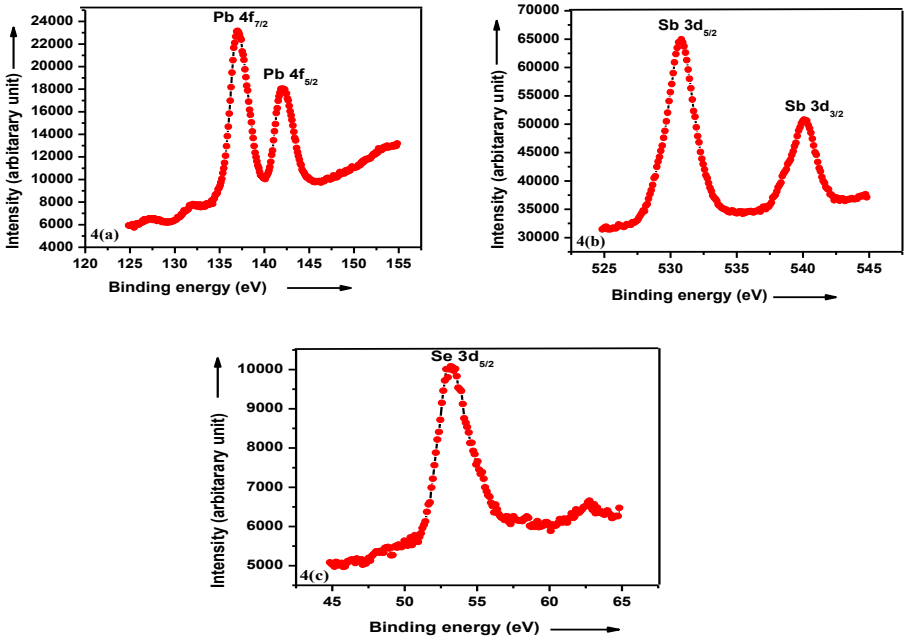


Fig. 4. XPS spectra for $Pb_{3.58}Sb_{4.42}Se_{10}$ film on glass substrate.

The two-dimensional (2D) and three-dimensional (3D) typical AFM images of the thin film are shown in Figs. 5(a)-(b). The film exhibited closely packed well defined grains of sizes 60 to 90 nm in diameter, confirming the nanocrystalline structures for the films. The root mean square (RMS) value of surface roughness determined from 3D image is 5 nm. The surface of the as-prepared thin film is almost smooth.

### 3.3. *Optical analysis*

The Swanepoel method is used for extracting the optical parameters of the film. The refractive index is calculated in weak and medium absorption region and is extrapolated in strong absorption region by the Cauchy's equation [29-31]. Using the interference fringe pattern of the transmittance spectra as depicted in Fig. 7(b), refractive index $n(\lambda)$ is calculated and the extracted values are plotted in Fig. 6(a). With increasing of energy, the

refractive index of a typical film is increased from 5.07 to 6.43. The accompanying Cauchy's fit with photon energy is shown in Fig. 6(b).

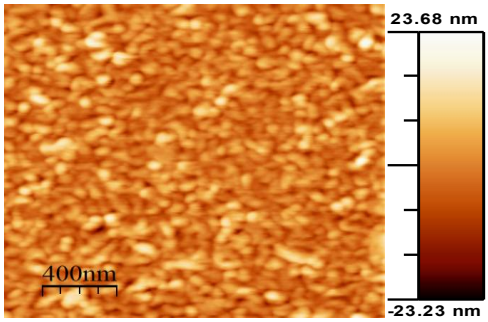


Fig. 5(a). The two dimensional AFM topography image of $Pb_{3.58}Sb_{4.42}Se_{10}$ thin film (area 2×2 μm )

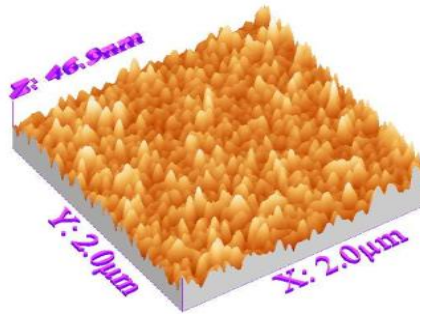


Fig. 5(b). the three dimensional AFM topography image of $Pb_{3.58}Sb_{4.42}Se_{10}$ thin film (area 2×2 μm).

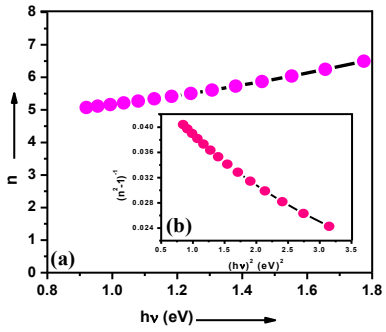


Fig. 6. Plots of (a) refractive index dispersion spectra of a typical sample with photon energy and (b) refractive index factor versus $(h\vartheta)^2$.

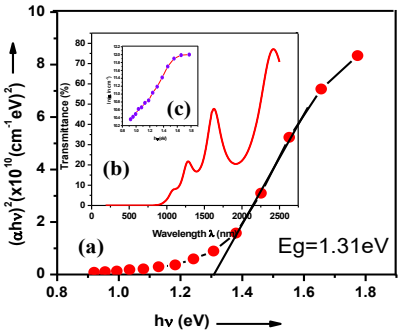


Fig. 7. Plot of (a) the dependence of $(\alpha h\vartheta)^2$ on photon energy for a typical $Pb_{3.58}Sb_{4.42}Se_{10}$ sample, (b) Typical transmission spectra and (c).

The thickness of the film $t$ can be calculated using the equation [32] as given by

$$t = \frac{\lambda_1 \lambda_2}{2(\lambda_1 n_2 - \lambda_2 n_1)} \quad (1)$$

where $n_1$ and $n_2$ are the refractive indices calculated from two consecutive maxima or minima corresponds to two wavelengths of $\lambda_1$ and $\lambda_2$. The thickness is found to be 600 nm and is well agreement with that obtained from the Stylus profiler. In the strong absorption region, the absorption coefficient $(\alpha)$ is found to be larger than $10^4$ $cm^{-1}$, which is very promising for photovoltaic application.

Absorption in a sample $(\alpha h\vartheta)^2$ versus photon energy is plotted according to Tauc's relation and is shown in Fig. 7(a). A linear region over a wide range of photon energy is found in the plot of $(\alpha h\vartheta)^2$ versus $h\vartheta$. It indicates that the dominant transition type is direct allowed. The optical band gap is found to be 1.31 eV. The plot of the natural logarithm of the absorption coefficient against the photon energy is shown in Fig. 7(c), it is found that

this tailing follows Urbach rule. The width of the tail is found to be 0.5 eV. It indicates the presence of structural disorder in the polycrystalline sample.

The single oscillator model proposed by the Wemple and DiDomenico (WDD) [33,34] is used to find the refractive index ($n$) as

$$n^2 - 1 = \frac{E_0 E_d}{E_0^2 - (h\vartheta)^2} \quad (2)$$

where $E_d$ is the dispersion energy and $E_0$ is the single-oscillator energy. The refractive index factor $(n^2 - 1)^{-1}$ versus $(h\vartheta)^2$ near the absorption edge is plotted and the data to a straight line (Fig. 6(b)) is fitted. The obtained values of WDD parameters $E_0$ and $E_d$ for a typical sample are 2.65 eV and 61.35 eV. As was proposed by Tanaka [35], the approximate value of the optical band gap $E_g$, is also derived from WDD model, according to the expression $E_g \approx \frac{E_0}{2}$. The value obtained is almost in agreement with that from the Tauc's extrapolation model. Fig. 8 shows the values of extinction coefficient ($k$) increases with increase in the photon energy and it varies from 0.34 to 0.91.The real part ($\varepsilon_r$) and imaginary part ($\varepsilon_i$) of the complex dielectric constant of the prepared film are also calculated [36] and their dependence on photon energy is presented in Fig. 9.

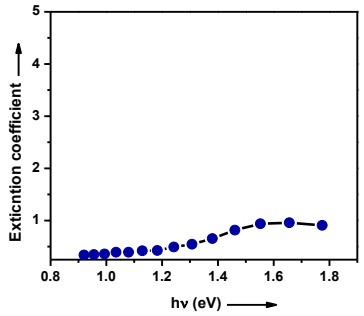


Fig. 8. Variation in $k$ with photon energy.

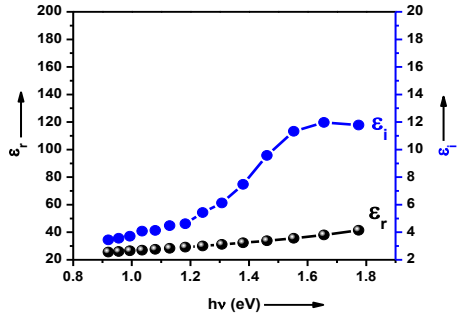


Fig. 9. Variation in $\varepsilon_r$ and $\varepsilon_i$ with photon energy.

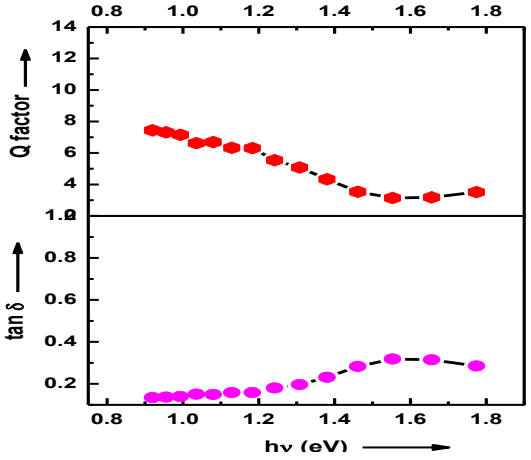


Fig. 10. Variation in tan $\delta$ and Q factor with photon energy

The dissipation factor (tan $\delta$) and Q factor of the films as a function of photon energy are shown in Fig. 10. The tan $\delta$ is the energy dissipation in the dielectric system, which is proportional to the imaginary part of the dielectric constant. tan $\delta$ is low at low photon energy and it increases with increasing energy.

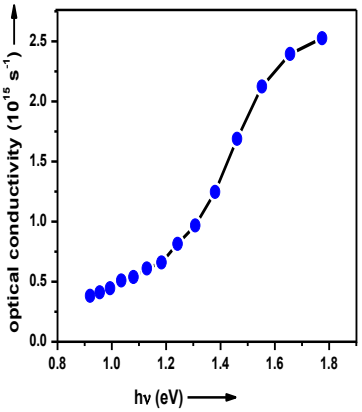


Fig. 11. The $\sigma_{opt}$ against photon energy for the $Pb_{3.58}Sb_{4.42}Se_{10}$ thin film sample.

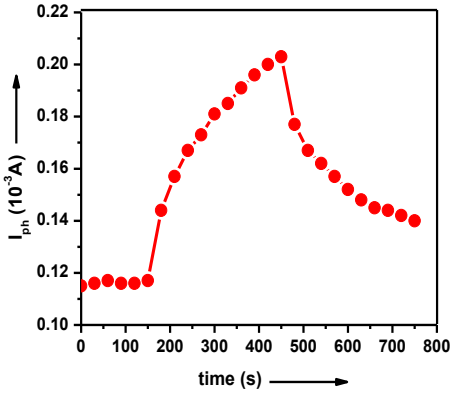


Fig. 12. The rise and decay of photocurrent in $Pb_{3.58}Sb_{4.42}Se_{10}$ film at room temperature.

The variation of optical conductivity for a $Pb_{3.58}Sb_{4.42}Se_{10}$ thin film is shown in Fig. 11 as a function of photon energy. It is found that $\sigma$ increases with increase in photon energy. The optical conductivity ($\sigma_{opt}$) of the film is obtained [32] by

$$\sigma_{opt} = \frac{\alpha n c}{4\pi} \tag{3}$$

where $\alpha$ is the absorption coefficient, $n$ is the refractive index and $c$ is the velocity of light. The high magnitude of optical conductivity ($>10^{14}$ $s^{-1}$) and the low extinction coefficient ($<1$) confirms the presence of very high photo response nature of the material. Fig. 12 reports the experimental results of time dependent transient photoconductivity measurements of a typical sample, there is an increase in the conductivity of the sample under illumination. The photocurrent first decreases rapidly after turning off the light and then decreases much more slowly. The photocurrent does not go to zero even after decaying for 350 s. The present photoconductivity rise and decay with time indicate that the photoconductivity behavior may be best understood in terms of deep traps within localized states

The differential lifetime is calculated using the Fuhs and Stuke relation for the analysis of decay rates in non-exponential decay [37]. The increase in differential life time with time shown in Fig. 13. It illustrates that the decay is non-exponential in nature. The slow decay may be ascribed due to deep traps that exist at all the energies in the band gap.

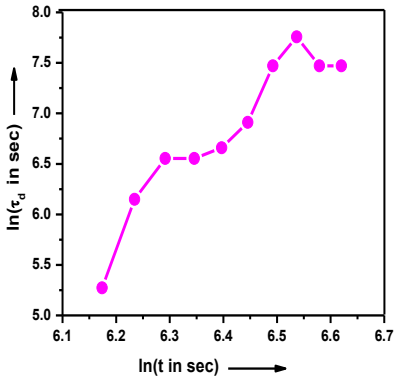


Fig. 13. The variation of differential life time.

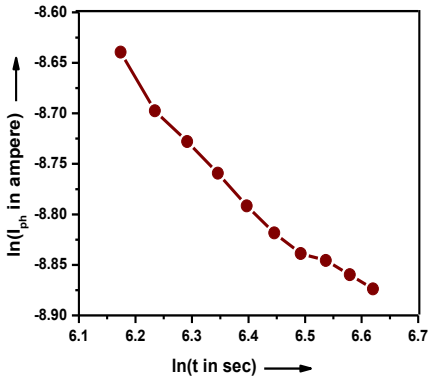


Fig. 14. The plot of ln ($I_{ph}$) versus ln(t).

From the slope of ln ($I_{ph}$) versus ln (t) (Fig. 14) the dispersion parameter ($\beta$) is calculated. Using the value of $\beta$, the localized state distribution parameter $E_l$ is also calculated. The obtained value of $E_l$ obtained is 0.0508 eV which gives the position of trap states in the band gap of the material. Unfortunately, we could not find any article that calculates the above reported parameters for $Pb_{3.58}Sb_{4.42}Se_{10}$ thin film. Hence, the values reported here could not be compared with others. The above results show that the reactively evaporated $Pb_{3.58}Sb_{4.42}Se_{10}$ thin films which display good electrical and optical properties, making it highly suitable for optoelectronic applications.

### 3.4. *Low temperature TEP properties and Hall measurement*

In a magnetic field of 0.55 T, the van der Pauw technique was used to obtain hall measurement (Table 4). The type of conductivity of the samples was checked using the hot probe method , the films showed p-type conductivity.

Table 4. Room temperature Hall measurement results.

| Carrier conc. $n$ ($cm^{-3}$) | Mobility $\mu$ ($cm^2V^{-1}s^{-1}$) | Hall coefficient $R_H$($cm^3C^{-1}V^{-1}$) | Magnetoresistance Ω (Ω) | Conductivity $\sigma$ ($\Omega^{-1}cm^{-1}$) |
|---|---|---|---|---|
| $\sim 1.263 \times 10^{13}$ | $\sim 38.48$ | $\sim 4.942 \times 10^{5}$ | $\sim 5.544 \times 10^{6}$ | $\sim 7.78 \times 10^{-5}$ |

Thermoelectric energy conversion at lower temperatures (around and below 300 K) can benefit a wide range of applications including refrigeration, air conditioning, and cryogenic cooling (17) but is also challenging mainly because the diffusive Seebeck coefficient drops in magnitude whereas the thermal conductivity increases as the temperature decreases. It is therefore tempting to make use of the phonon drag effect to boost the Seebeck coefficient for better thermoelectrics at lower temperatures [38]. The variation of Seebeck coefficient $S$ of $Pb_{3.58}Sb_{4.42}Se_{10}$ film in the temperature range of 11-300K is depicted Fig. 15.

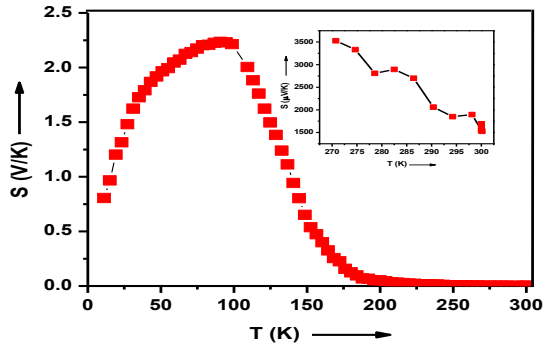


Fig. 15. The variation of the TEP with temperature.

The variation of Seebeck coefficient was found to be positive indicating the predominant p-type behavior of $Pb_{3.58}Sb_{4.42}Se_{10}$ film. Figur shows that $S$ is slightly varying in the range 1691 μVK$^{-1}$ to 3332 μVK$^{-1}$ from 300 K to 273 K which is a typical behaviour of a non-degenerate semiconductor (Fig. 15). It is found that $S$ starts to increase abruptly as temperature decreases and the film shows a giant Seebeck coefficient of 2.23 VK$^{-1}$ at about 90 K. The peak at 90 K indicates the presence of substantial phonon drag effects in this sample contributing to a giant Seebeck coefficient at low temperature. Below 90 K the thermoelectric power decreases rapidly. For non-degenerate semiconductors [39],

$$S = \pm\frac{k_B}{e}\left[A + \frac{E_F}{k_B T}\right] \quad (4)$$

where $E_F$ is the separation of the Fermi level from the top of the valence band, $e$ is the charge of the electron and $k_B$ is the Boltzmann's constant. $A = \left(\frac{5}{2} - s\right)$ is transport term, a constant varies from 0 to 4 depends on the scattering process. The calculated value of scattering parameter $A$ is found to be 2, indicates the presence of acoustic phonon scattering.

Table 5 The semiconductor properties of $Pb_{3.58}Sb_{4.42}Se_{10}$ film at Fermi level.

| Fermi level $E_F$ (eV) | Effective mass $m^*$ | Density of states $N$ (cm$^{-3}$) | Relaxation time $\tau$ (s) | Fermi velocity $v_F$ (m s$^{-1}$) | Mean free path $l$ (nm) |
|---|---|---|---|---|---|
| ~ 0.454 | ~ 0.00044 $m_0$ | ~2.29 × $10^{14}$ | ~ 0.096 × $10^{-16}$ | 1.9× $10^{7}$ | ~ 18.24 |

It is found that the Fermi level lies deep in the band gap of the material (Table 5). The electrical conductivity of 7.786×10$^{-5}$ Ω$^{-1}$cm$^{-1}$ and the Seebeck coefficient of 1691 μVK$^{-1}$ at room temperature gives that the prepared film has a moderate power factor of 2.23×10$^{-8}$ Wcm$^{-1}$K$^{-2}$. The effective mass (0.00044 $m_0$) is found to be low, the low electrical conductivity is due to the low carrier concentration. The power factor at room temperature is lower than those of state-of-the-art thermoelectric materials, the giant $S$ value at low temperature can be prospectively beneficial for low temperature applications with high performance [40-42].

## 4. Conclusion

Here the optical and transport properties are reported for reactively evaporated p-type nano-structured lead antimony selenide ($Pb_{3.58}Sb_{4.42}Se_{10}$) thin films. From the XRD pattern of the as prepared film, the structural parameters such as dislocation density, number of crystallites per unit area and lattice strain in a typical film are estimated and are reported as $1.6\times10^{15}$ lines $m^{-2}$, $3.84\times10^{14}$ $m^{-2}$ and $2.267\times10^{-3}$. The obtained average particle size is 25 nm. The conductivity is of the order of $7.78 \times 10^{-5}$ $\Omega^{-1}cm^{-1}$ and it is of p-type. The high absorbance ($>10^4$ $cm^{-1}$), optical band gap of 1.31 eV and high optical conductivity reported here for $Pb_{3.58}Sb_{4.42}Se_{10}$ thin films suggests the possible application of these films as absorber layer in solar cell. At 90 K a maximum TE power of 2.3 $VK^{-1}$ occurs. A relatively higher $S$ of about 1691 $\mu VK^{-1}$ is exhibited at room temperature. All these results are promising in the realization of room temperature and even lower temperature thermoelectric application with high performance. The combination of both optical and TE properties of $Pb_{3.58}Sb_{4.42}Se_{10}$ thin films make them more prominent for PV-TE hybrid system and also for a variety of other PV-TE applications.

## Acknowledgments

Authors are grateful to Department of Physics, Cochin University of Science and Technology for providing XRD, UV Vis NIR spectrophotometer facility. Authors also gratefully acknowledge V. Ganesan and G. S. Okram, UGC-DAE Consortium for Scientific Research, Indore, India for extending AFM and thermoelectric power measurements facilities. Thanks, are also to DST- FIST for providing HMS 3000 for Hall effect measurements at Sree Narayana College Nattika.

## References

1. K.-T. Park, S.-M. Shin, A. S. Tazebay, H.-D. Um, J.-Y. Jung et al., Sci. Reports **3**, ID 2123 (2013). https://doi.org/10.1038/srep02123
2. Sima Aminorroaya-Yamini, C. Zhang, X. Wang and I. Nevirkovets, J. Phys. D Appl. Phys. **45**, ID 125301 (2012). https://doi.org/10.1088/0022-3727/45/12/125301
3. C. Wood, Rep. Prog. Phys. **51**, 459 (1988). https://doi.org/10.1088/0034-4885/51/4/001
4. G. S. Nolas, M. Kaeser, R. T. Littleton and T. M. Tritt, Appl. Phys. Lett. **77**, 1855 (2000). https://doi.org/10.1063/1.1311597
5. X. Shi, J. Yang, J. R. Salvador, M. Chi, J. Y. Cho et al., J. Am. Chem. Soc. Chem. Soc. **133**, 7837 (2011). https://doi.org/10.1021/ja111199
6. G. S. Nolas, T. D. Morelli and T. M. Tritt, Annu. Rev. Mater. Sci. **29**, 89 (1999). https://doi.org/10.1146/annurev.matsci.29.1.89
7. P. Norouzzadeh, C. Myles and D. Vashaee, Sci. Reports **4**, ID 7028 (2014). https://doi.org/10.1038/srep07028
8. T. Takabatake, K. Suekuni, T. Nakayama and E. Kaneshita, Rev. Mod. Phys., **86**, 669 (2014). https://doi.org/10.1103/RevModPhys.86.669
9. G. S. Nolas, J. L. Cohn, G. A. Slack and S. B. Schujman, Appl. Phys. Lett. **73**, 178 (1998). https://doi.org/10.1063/1.121747
10. G. S. Nolas and G. A. Slack, Sigma Xi, Sci. Res. Soc. **89**, 136 (2001).

https://doi.org/10.1511/2001.20.136
11. J. W. Simonson, D. Wu, W. J. Xie and S. J. Poon, Phys. Rev. B **83**, ID 235211 (2011). http://dx.doi.org/10.1103/PhysRevB.83.235211
12. T. M. Tritt, Science **283**, ID 804 (1999). https://doi.org/10.1126/science.283.5403.804
13. G. S. Nolas, J. Poon, and M. Kanatzidis, MRS Bull. **31**, 199 (2006). https://doi.org/10.1557/mrs2006.45
14. D. Chung, T. Hogan, P. Brazis, R. Melissa, C. Kannewurf et al., Science **287**, 1024 (2000). https://doi.org/10.1126/science.287.5455.1024
15. Y. Pei, X. Shi, A. Lalonde, H. Wang, L. Chen et al., Nature **473**, 66 (2011). https://doi.org/10.1038/nature09996
16. N. Chen, F. Gascoin, G. J. Snyder, E. Muller, G. Karpinski et al., Appl. Phys. Lett. **87**, 17190 (2005). https://doi.org/10.1063/1.2056590
17. S. D. Mahanti, P. Larson, Duck-Young Chung, S. Sportouch and M. G. Kanatzidis, Mat. Res. Soc. Symp. Proc. **545**, 23 (1998). https://doi.org/10.1557/PROC-545-23
18. K. Koumoto, I. Terasaki and R. Funahashi, MRS Bull. **31**, 206 (2006). http://dx.doi.org/10.1557/mrs2006.46
19. H. Böttner, G. Chen, and R. Venkatasubramanian, MRS Bull. **31**, 211 (2006). https://doi.org/10.1557/mrs2006.47
20. M. G. Kanatzidis, Chem. Mater. **22**, 648 (2010). https://doi.org/10.1021/cm902195j.
21. D. Hitchcock, Yen-Liang Liu, Y. Liu, M. Terry, H. Jian et al., Funct. Mater. Lett. **06**, ID 1340008 (2013). https://doi.org/10.1142/S1793604713400080.
22. W. Xie, S. Wang, S. Zhu, H. Jian, X. Tang et al., J. Mater. Sci. **48**, 2745 (2013). https://doi.org/10.1007/s10853-012-6895-z
23. L.-H. Ye, K. Hoang, A. J. Freeman, S. D. Mahanti, H. Jian et al., Phys. Rev. B **77**, ID 245203 (2008). https://doi.org/10.1103/physrevb.77.245203.
24. N. S. Patil, A. M. Sargar, S. R. Mane and P. N. Bhasale, Mater. Chem. Phys. **115**, 47 (2009). https://doi.org/10.1016/j.matchemphys.2008.11.026
25. J. Kim, J. Choi, J. Bae, M. Kim and T. Oh, Mater. Trans. **54**, 618 (2013). https://doi.org/10.2320/MATERTRANS.M2013010
26. B. Parida, S. Iniyan, and R. Goic, Renew. Sustain. Energy Rev. **15**, 1625 (2011). https://doi.org/10.1016/j.rser.2010.11.032
27. Powder Diffraction file, International Centre for Diffraction Data (ICDD) Card No: 80-0654.
28. N. S. Devi, M. R. Shiekh, L. R. Singh, and A. N. Singh, J. Sci. Res. **16**, 745 (2024). https://doi.org/10.3329/jsr.v16i3.72000
29. A. F. Qasrawi, Opt. Mater. **29**, 1751 (2007). https://doi.org/10.1016/j.optmat.2006.09.009
30. A. K. S. Aqili, Z. Ali, and A. Maqsood, Appl. Surf. Sci. **167**, 1 (2000). https://doi.org/10.1016/S0169-4332(00)00498-0
31. E. Marquezt, J. Ramirez-Malot, P. Villarest, R. Jimenez – Garay, P. J. S. Ewen et al., J. Phys. D Appl. Phys. **25**, 535 (1992). https://doi.org/10.1088/0022-3727/25/3/031
32. E. R. Shaabana, I. S. Yahiab, and E. G. El-Metwally, Acta Phys. Pol. A **121**, 628 (2012). https://doi.org/10.12693/APhysPolA.121.628
33. S. H. Wemple and M. DiDomenico, Phys. Rev. B **3**, 1338 (1997). https://doi.org/10.1103/PHYSREVB.3.1338
34. S. H. Wemple and M. DiDomenico, Phys. Rev. Lett. **23**, 1156 (1969). https://doi.org/10.1103/PhysRevLett.23.1156
35. K. Tanaka, Thin Solid Films **66**, 271 (1980). https://doi.org/10.1016/0040-6090(80)90381-8
36. S. M. El-Sayed, Vacuum **72**, 169 (2003). https://doi.org/10.1016/S0042-207X(03)00139-8
37. A. Kumar, S. Goel, and S. K. Tripathi, Phys. Rev. B **38**, 432 (1988). https://doi.org/10.1103/PhysRevB.38.13432
38. J. Zhou, B. Liao, B. Qiu, and G. Chen, PNAS **112**, 14777 (2015). https://doi.org/10.1073/pnas.1512328112
39. K. P. Mohanchandra and J. Uchil, Thin Solid Films **305**, 124 (1997). https://doi.org/10.1016/S0040-6090(97)00188-0

40. X. Zhang and L. Zhao, J. Materiomics **1**, 92 (2015). https://doi.org/10.1016/j.jmat.2015.01.001
41. T. Rasmi, Rapaka S. Chandra Bose, T. S. Varun, Pramod Aarya, Ponnada Aarya et al., J. Alloys Compd. **1034**, ID 181378 (2025). https://doi.org/10.1016/j.jallcom.2025.181378
42. M. Kim, D. Park, and J. Kim, Mater. Chem. Phys. **337**, ID 130571 (2025). https://doi.org/10.1016/j.matchemphys.2025.130571